

Segmentation of MR images with intensity inhomogeneities

Jagath C. Rajapakse*, Frithjof Kruggel

Max-Planck-Institute of Cognitive Neuroscience, Leipzig, Germany

Received 4 November 1996; revised 5 September 1997; accepted 23 September 1997

Abstract

A statistical model to segment clinical magnetic resonance (MR) images in the presence of noise and intensity inhomogeneities is proposed. Inhomogeneities are considered to be multiplicative low-frequency variations of intensities that are due to the anomalies of the magnetic fields of the scanners. The measurements are modeled as a Gaussian mixture where inhomogeneities present a bias field in the distributions. The piecewise contiguous nature of the segmentation is modeled by a Markov random field (MRF). A greedy algorithm based on the iterative conditional modes (ICM) algorithm is used to find an optimal segmentation while estimating the model parameters. Results with simulated and hand-segmented images are presented to compare performance of the algorithm with other statistical methods. Segmentation results with MR head scans acquired from four different clinical scanners are presented. © 1998 Elsevier Science B.V.

Keywords: Bias field; Brain imaging; Magnetic resonance images; Image segmentation; Intensity inhomogeneities; Statistical modeling

1. Introduction

Many clinical and research applications using magnetic resonance (MR) images require a segmentation into different intensity classes which are regarded as the best available representations for biological tissues. Segmentation of MR head scans is a prerequisite for three-dimensional visualization of brain surface and structures, surgery planning and guidance, detection of anatomical structures in brain morphometry, defining targets in radioactive therapy treatment and planning and derivation of brain anatomical atlases [1–3]. Manual segmentation of MR scans is both time-consuming and inconsistent and affected by operator bias [4,5]. A major obstacle to any automated method of segmentation of MR images is the presence of spatial intensity inhomogeneities [6]. We refer to *intensity inhomogeneities* as nonuniformities of intensities over the same class of tissues or structures, which are not caused by random noise.

Intensity inhomogeneities in MR images occur due to a number of reasons: (1) the irregularities of the scanner magnetic fields – static (B_0), radio-frequency (B_1) and gradient fields [7–11]; (2) the variations of magnetization properties (susceptibility) of the biological tissues [8,9]; (3) the differential attenuation of signals due to the location of the structures; and (4) other nonlinearities in the scanners

(sensitivities of the receiver coils, operating conditions, the age and status of the MR equipment, etc.) [10,12,13]. The majority of the intensity inhomogeneities are caused due to reason (1) and appear as low-frequency intensity variations across the field of view and from slice to slice [5]. The severity of the inhomogeneities mostly depends on the quality of the scanner characteristics.

Because the characteristics of the sources creating intensity inhomogeneities are not easily known, deterministic methods cannot be designed to account for the inhomogeneities in MR images. Although phantom studies have been performed to assess the inhomogeneity profile of a particular scanner [5,13,14], such studies have several drawbacks. The most difficult problem is to construct phantoms to simulate the human body with its complex tissue compartments and properties. Because the characteristics of the scanners vary with time and use, ideally a phantom should be imaged with every scanned object under the same conditions. Such studies are not feasible for longitudinal or developmental studies involving a large number of scans.

A review of current methods for MR image segmentation can be found in Refs [15,16]. Most classical image processing techniques such as edge and region detection schemes fail to segment MR images satisfactorily because of the lack of clear edges. Thresholding of the image contrast is not feasible because of the overlapping of the tissue intensity distributions, the spatial variations in MR characteristics of the same tissue class and the presence of signal

* Corresponding author. Tel: 0049 3419 940 225; Fax: 0049 341 9940 221; e-mail: raja@cns.mpg.de

nonuniformities. Statistical segmentation techniques have been proposed to overcome errors due to inhomogeneities [3,5–9,11,17,18], but tested on images from a single scanner. Attempts to model inhomogeneity profiles with basis functions [5] and polynomials [6] have not considered the randomness of the inhomogeneities. An extension to the fuzzy-c-means clustering algorithm was presented to overcome inhomogeneities [7], but the method requires initialization of parameters using a set of previous scans. A gain field related to the inhomogeneities was derived in [8,9] from log-transformed image data using the expectation–minimization (EM) algorithm [19]. A homomorphic filter was used to remove slowly varying components of the inhomogeneities [17], but such a method corrupts high-frequency details in the image. Differences between local and global median characteristics were used to correct the intensity profile of the images [18]. All the aforementioned methods have not been tested for segmentation of images acquired over a wide range of imaging conditions and in different MR scanners and none utilizes a prior model to represent the connectivities seen in the segmentations.

A statistical scheme for the segmentation of MR images in the presence of noise and intensity inhomogeneities will be presented in the following. Noise and inhomogeneities are explicitly incorporated to a measurement model and the connectivity and neighborhood correlations in a segmentation to a prior model. The tissue classes are modeled with Gaussian distributions and the prior of the segmentation is modeled with a Markov random field (MRF). Imperfections in the RF coil correspond to a pointwise multiplication of ideal image intensities with a bias that varies slowly spatially [9]. The inhomogeneities are considered to present a multiplicative *bias field* over the image as assumed by others [7–9], which poses low-frequency intensity nonuniformities over the image independent of the tissue classes.

With the present model, the optimal segmentation is derived as the maximum a posteriori probability (MAP) estimation [20,21] given the image data. A local minimum of the associated energy function in the posterior probability is sought as an approximation to the optimal segmentation using a greedy algorithm based on the iterative conditional modes (ICM) algorithm [22]. Expressions to estimate the model parameters as maximum-likelihood (ML) estimates [23] using the image data and segmentation results in an iterative manner are presented. Although a similar segmentation scheme based on the ICM algorithm was recently proposed for segmentation of two-dimensional MR images, the effects of inhomogeneities were not taken into account [24].

In some applications, the outer hulls of the brain (i.e. background, skull, muscles, meninges, etc.) are removed from the MR head scans prior to the segmentation. We will refer the process of extracting the brain parenchyma from the head scans as *shelling* or *peeling* and the term *head scan* will be used to refer to the original image before the peeling process unless otherwise specified. Peeled head

scans are usually segmented into three classes, namely gray matter, white matter and cerebrospinal fluid (CSF), whereas the segmentation of head scans is more complicated due to the presence of the large number of other intensity classes such as background, bone, muscles, fat, etc. In a previous report [3], we utilized local characteristics to model the intensity variations of the tissue classes and determined local tissue parameters using a brute-force technique – computing means and variances of each tissue class at every voxel site using a sufficiently large neighborhood to segment shelled brain images. We will refer our earlier approach as *adaptive* MAP (AMAP) because the parameters of the tissues are adapted spatially for segmentation. An arbitrary model is assumed for the effects of intensity inhomogeneities in the AMAP algorithm. The major impediment to the practical use of the AMAP algorithm is its formidable computational and memory requirements which increase with the number of tissue classes, precluding it being used for segmentation of three-dimensional head scans without peeling them by other means. The present method evolved as a result of our search for a pragmatic scheme for the segmentation of three-dimensional head scans. In the present approach, we model the scanner intensities as a slow varying bias field which interacts with the tissue properties in a multiplicative manner to produce tissue intensities. As seen in the sequel, the multiplicative model renders us analytical expressions for the parameters of tissue classes, leading to an alternative and more efficient algorithm to the AMAP algorithm while preserving the quality of segmentation, which is especially fruitful when MR head scans need to be segmented into a large number of tissue classes. Because of the bias field involved, the proposed algorithm is referred as biased-MAP or BMAP. With simulated images, it will be shown that the BMAP algorithm outperforms the existing statistical schemes as the intensity of the inhomogeneities increases.

In Section 2, the statistical model for MR images will be introduced. Section 3 describes the segmentation algorithm which finds a suboptimal segmentation and estimates the model parameters. In Section 4, results of segmentations with the BMAP algorithm on MR head scans from four different scans are shown. In addition, a synthetic two-dimensional MR image with known inhomogeneity profile is used to compare the efficacy of the proposed method with other statistical schemes and comparison of the performances of the AMAP and BMAP algorithms with hand-segmented images is presented. Section 5 discusses the results and limitations of our segmentation scheme.

2. Image model

A three-dimensional MR head scan which consists of a set of contiguous voxels is considered. Let the sites of image voxels be represented by three-dimensional Cartesian coordinates $i \in I$ and the set of voxel sites be denoted by $I \subset \mathbb{N}^3$. The image is denoted by $\mathbf{y} = (y_i; i \in I)$ where y_i is the

intensity of the voxel at site i . Let us assume that the image consists of K different classes of biological tissues and structures and each voxel consists of brain matter belonging to only a single class. The number of classes in the model can be easily increased as proposed in Ref. [25] to include the effects of partial voluming. Segmentation refers to the process of assigning the corresponding tissue class label to each image voxel. If the space of the tissue classes is $\Lambda = \{1, 2, \dots, K\}$ and x_i represents the tissue class of the voxel at the image site i , $x_i = k$ denotes an assignment of the k th tissue class to the site i . A segmentation of the image is given by $\mathbf{x} = (x_i; i \in I)$.

The *measurement model* of the image is given by:

$$y_i = (1 + \beta_i)\mu_{x_i} + \eta_i, \quad (1)$$

where μ_{x_i} denotes the mean intensity of the tissue class, η_i denotes the random noise signal and β_i represents the variation of the gain of the intensity due to the intensity inhomogeneities at the site i . The inhomogeneities are considered to be multiplicative with the tissue intensities and depend on the location. The noise is assumed to be class-conditional and the noise distribution for each class to be additive, random, white and Gaussian [26,27]. That is, if $x_i = k$, then $\eta_i \sim N(0, \sigma_k^2)$ where σ_k^2 is the variance of the noise for the tissue class k . The class conditional probability at the voxel site i is written as:

$$p(y_i|x_i = k) = \frac{1}{\sqrt{2\pi\sigma_k^2}} \exp\left\{-\frac{1}{2}\left(\frac{y_i - (1 + \beta_i)\mu_k}{\sigma_k}\right)^2\right\}, \quad (2)$$

where the vector $\beta = (\beta_i; i \in I)$ represents the bias field.¹ If $\theta_k = (\mu_k, \sigma_k)$ and $\theta = (\theta_k; k \in \Lambda)$, the measurement model parameters are given by (β, θ) .

The *prior model* of the segmentation is considered to be a three-dimensional MRF which models the piecewise contiguous nature of the image elements considering that the adjacent voxels are more likely to have similar constituents and belong to the same tissue class. According to the Hammersly–Clifford theorem [28], the prior probability of an MRF is given by a Gibb's distribution [20]. Therefore, the prior model of the segmentation is given by:

$$p(\mathbf{x}) = \frac{1}{Z} \exp\left\{-\sum_{c \in C} V_c(\mathbf{x})\right\}, \quad (3)$$

where Z is the normalizing constant and the summation is taken over the prior potentials $V_c(\mathbf{x})$ for the set of cliques C over the image. A clique is a set of voxels that are neighbors of one another. We use the multilevel logistic (MLL) model [29] of Gibb's distributions, where a parameter gives the potential for the interactions among the sites for each clique irrespective of the classes of its constituents. For simplicity, we restrict our attention to the interactions due to *singletons* (one-site cliques) and *doubletons* (two-site cliques).

The potential energy of the MRF may be written as:

$$\sum_{c \in C} V_c(\mathbf{x}) = \sum_{i \in I} \{V_1(x_i) + V_2(x_i)\}, \quad (4)$$

where $V_1(\cdot)$ and $V_2(\cdot)$ are the potentials of singletons and doubletons, respectively, and the local potentials are given by

$$V_1(x_i) = \sum_{k \in \Lambda} -\alpha_{0k} \delta(x_i = k), \quad (5)$$

$$V_2(x_i) = \sum_{i, j \in c_i} \{-\alpha_l \delta(x_i = x_j) + \alpha_l \delta(x_i \neq x_j)\}, \quad (6)$$

where $\delta(\cdot)$ takes value one when the condition is satisfied, otherwise zero. The real constant α_{0k} represent the potential for the singleton for the k th tissue class and α_l gives the potential for the interaction of the doubletons c_l in the l th-order neighborhood which is defined for the site i as the set $\{j: |i - j| \leq \sqrt{l}, j \in I, j \neq i\}$. Because of computational difficulties, neighborhoods are considered up to the second-order when computing the clique potentials. Therefore, the prior model parameters are given by $\alpha = (\alpha_{0k}, \alpha_1, \alpha_2; k \in \Lambda)$. The first-order neighborhood in three dimensions consists of six of its nearest neighbors and the second-order neighborhood consists of 18 nearest neighbors.

We attempt to find the segmentation giving the MAP estimates [20] rendered by the image data. That is, the optimal segmentation $\mathbf{x} = \mathbf{x}^*$ is given by:

$$\mathbf{x}^* = \arg \max_{\mathbf{x}} p(\mathbf{x}|\mathbf{y}). \quad (7)$$

Because the prior probability of the image $p(\mathbf{y})$ is independent of the segmentation, from Bayes' theorem, the posterior probability of the segmentation $p(\mathbf{x}|\mathbf{y})$ can be written as:

$$p(\mathbf{x}|\mathbf{y}) \propto p(\mathbf{y}|\mathbf{x})p(\mathbf{x}). \quad (8)$$

By substituting Eq. (8) in Eq. (7) and indicating the dependencies of the probability densities on the model parameters, one can write:

$$\mathbf{x}^* = \arg \max_{\mathbf{x}} p(\mathbf{y}|\mathbf{x}, \beta^*, \theta^*)p(\mathbf{x}|\alpha^*), \quad (9)$$

where (β^*, θ^*) and α^* denote the optimal measurement and prior model parameters, respectively. The vector β represents the bias field due to the inhomogeneities, θ is made up of means and standard deviations of the tissue intensity distributions and α gives the likelihoods of interactions among neighboring voxels. In order to find the optimal segmentation, it is necessary to devise a segmentation scheme which finds the optimal model parameters as well.

3. Segmentation algorithm

Because the noise in the measurements is white, the image data are conditionally independent.

¹ In [8] and [9], $(1 + \beta_i)$ was referred to as *bias field* which we prefer to refer as *gain field* [7].

That is:

$$p(\mathbf{y}|\mathbf{x}) = \prod_{i \in I} p(y_i|x_i). \quad (10)$$

From Eqs. (2–4), (8) and (10) and neglecting the constant terms, one can write:

$$p(\mathbf{x}|\mathbf{y}) \propto \exp\{-U(\mathbf{x}|\mathbf{y})\}, \quad (11)$$

where the global energy function $U(\mathbf{x}|\mathbf{y}) = \sum_{i \in I} U_i(x_i|x_j, y_i, j \neq i)$ and the local energies at voxel sites $i \in I$ are given by:

$$U_i(x_i|x_j, y_i, j \neq i) = \frac{1}{2} \left(\frac{y_i - (1 + \beta_i)\mu_{x_i}}{\sigma_{x_i}} \right)^2 + \log(\sigma_{x_i}) + V_1(x_i) + V_2(x_i). \quad (12)$$

The MAP estimator of the segmentation minimizes the energy function $U(\mathbf{x}|\mathbf{y})$. Estimation of \mathbf{x} corresponding to the minimum global energy in Eq. (11) is a difficult energy minimization task which is compounded by unknown model parameters. Therefore, we attempt to find a suboptimal solution to the MAP segmentation while estimating the model parameters. This approach can be expressed in the following steps:

$$\hat{\mathbf{x}} = \arg \min_{\mathbf{x}} U(\mathbf{x}|\mathbf{y}, \hat{\beta}, \hat{\theta}, \hat{\alpha}), \quad (13)$$

$$(\hat{\beta}, \hat{\theta}) = \arg \max_{\beta, \theta} p(\mathbf{y}|\hat{\mathbf{x}}, \beta, \theta), \quad (14)$$

$$\hat{\alpha} = \arg \max_{\alpha} p(\alpha|\hat{\mathbf{x}}), \quad (15)$$

where the hat indicates an estimation. The measurement model parameters are chosen to maximize the likelihood of the image data and the prior model parameters are optimized for a given segmentation. No known solution exists to solve the above simultaneous optimization problem (Eqs. (13)–(15)). We present further on an iterative greedy algorithm based on the ICM algorithm [22], which finds an approximation to the MAP estimation of the segmentation. At each iteration, the measurement model parameters are evaluated using the segmentation results of the previous iteration. Because the bias field is involved in the model, we will refer to the present segmentation scheme as the *biased MAP* (BMAP) criterion.

The BMAP algorithm is essentially a *segmentation-estimation* scheme [30] which starts with an initial segmentation and iteratively evolves alternating between segmentation and parameter evaluation processes. With the known model parameters, the tissue class is assigned at every voxel site to maximize the local energy. That is:

$$\hat{x}_i = \arg \min_{x_i} U_i(x_i|x_j, y_i, \hat{\beta}, \hat{\theta}, \hat{\alpha}, j \neq i). \quad (16)$$

After assignment of class labels to all the sites, the model parameters are recomputed. With these parameters, it reclassifies the image voxels in the next cycle minimizing

the local energies. This process is iterated until the algorithm converges, which is achieved when there are no more changes in the class labels or *flips* at the image sites.

3.1. Initialization

Initialization is an important part of the segmentation scheme because the algorithm finds only a local minimum of the global energy function. In order to initialize the parameters, a simplified image model is considered with no bias field and prior and equal noise variances for the tissue classes. Therefore, the initial energy function $U(\cdot) = U^0(\cdot)$ is given by:

$$U^0(\mathbf{x}|\mathbf{y}) = \sum_{k \in \Lambda} \sum_{i \in R_k} (y_i - \mu_k)^2, \quad (17)$$

where the set of all points that belong to the class k in the image is $R_k = \{i : x_i = k, i \in I\}$. The *k-means* algorithm can be used to find the initial segmentation \mathbf{x} minimizing the initial energy function $U^0(\cdot)$. To avoid the problem of initialization of the *k-means* algorithm, a *tree-structure k-means* algorithm (T_{sk} -means) [24] was employed in simulations. The algorithm starts with one class and the classes grow in a tree until the desired number of classes is achieved. At each stage, the class or the tree node which results in a minimum energy configuration is split to produce two new classes for the next stage. The class with mean μ is split by introducing a perturbation ϵ to produce two new classes with means $\mu - \epsilon$ and $\mu + \epsilon$. At the outset, the mean of the only class is made equal to that of the image and the perturbation is made proportional to the image standard deviation [31].

3.2. Estimation of prior model parameters

The prior model parameters are derived from the initial segmentation. Coding and pseudo-likelihood methods [21,22] to estimate MRF parameters lead to nonlinear iterative and tedious ML estimation schemes. Therefore, we follow a different approach. The singleton potentials represent the likelihood of each class, which are evaluated proportional to the number of the voxels belonging to the each tissue class. That is:

$$\hat{\alpha}_{0k} = \log \frac{|R_k|}{\sum_{j \in \Lambda} |R_j|}, \quad (18)$$

where $|R_k|$ denotes the number of sites with class label k in the image.

To find the doubleton potentials, consider a voxel pattern with the center voxel having class label k and the neighborhood having a pattern ' t ' which is characterized by the class labels of the neighborhood voxels. From Eqs. (3), (5) and (6), the probability for a configuration (k, t) is given by:

$$P(k, t) = \frac{1}{Z'} \exp\{\alpha_{0k} + 2\alpha_1(f_k - 3) + 2\alpha_2(s_k - 6)\}, \quad (19)$$

where f_k and s_k are the total number of k class voxels in the first-order neighborhood and in the second-order neighborhood excluding the first-order neighbors, respectively. Considering a configuration having any other class j at the center and the same neighborhood pattern 't' (i.e. corresponding neighborhood voxels having the same classes except a different class label at the center) and substituting j in Eq. (19), one can obtain:

$$\alpha_{0k} - \alpha_{0j} + 2\alpha_1(f_k - f_j) + 2\alpha_2(s_k - s_j) = \log \frac{P(k, t)}{P(j, t)} \quad (20)$$

If $n(k, t)$ and $n(j, t)$ are the numbers of configurations (k, t) and (j, t) in the initial segmentation, respectively, in order to maximize the likelihood, one can write $\hat{P}(k, t)/\hat{P}(j, t) = n(k, t)/n(j, t)$. Substituting this in Eq. (20), for any configuration where $n(k, t) > 0$ and $n(j, t) > 0$, a linear equation of α_1 and α_2 may be obtained with α_{0s} computed from Eq. (18). Because the number of possible equations is greater than the number of variables, the least-square estimates of α_1 and α_2 are evaluated minimizing the square error Δ given by:

$$\Delta = \sum_{i \in \Omega} \sum_{(k, j) \in \Lambda^2} (\alpha_1(f_k - f_j) + \alpha_2(s_k - s_j) - L_{k, j}(t))^2, \quad (21)$$

where $L_{k, j}(t) = \log(n(k, t)/n(j, t)) - \alpha_{0k} + \alpha_{0j}$, and Ω is the space of the neighborhood configurations.

3.3. Estimation of measurement model parameters

The measurement model parameters are estimated after the segmentation in each iteration. Instead of maximizing the likelihood in Eq. (14), the negative log-likelihood is minimized. From Eqs. (2) and (10), neglecting constant terms, for a given segmentation:

$$-\log P(\mathbf{y}|\hat{\mathbf{x}}, \boldsymbol{\beta}, \boldsymbol{\theta}) = \frac{1}{2} \sum_{k \in \Lambda} \sum_{i \in R_k} \left(\frac{y_i - (1 + \beta_i)\mu_k}{\sigma_k} \right)^2 + \sum_{k \in \Lambda} \sum_{i \in R_k} \log(\sigma_k). \quad (22)$$

By differentiating this equation with respect to μ_k and equating it to zero, the estimate of μ_k is given by:

$$\hat{\mu}_k = \frac{\sum_{i \in R_k} y_i(1 + \beta_i)}{\sum_{i \in R_k} (1 + \beta_i)^2}, \quad (23)$$

and similarly differentiating Eq. (22) with respect to σ_k

$$\hat{\sigma}_k^2 = \frac{\sum_{i \in R_k} (y_i - (1 + \beta_i)\hat{\mu}_k)^2}{|R_k|}. \quad (24)$$

The bias field values are obtained by differentiating Eq. (22) with respect to each β_i and equating it to zero:

$$\hat{\beta}_i = \frac{y_i}{\hat{\mu}_{x_i}} - 1.0. \quad (25)$$

$\hat{\beta}$ calculated using Eq. (25) may contain spurious noise resulted due to misclassifications in the current segmentation. To remove this noise, the bias field is filtered using a low-pass filter before the segmentation begins in the next cycle. Our experience indicates that a moving average filter is appropriate with a threshold to neglect spurious bias values during the averaging process. We set this threshold to 0.75 in all our experiments considering the maximum allowable nonuniformities recommended for clinical scanners [10]. A filter size equal to the scale of the inhomogeneities yields optimum results, which needs to be fixed considering the scale of the inhomogeneities and voxel dimensions. We will refer this filter as *bias filter*.

3.4. Implementation

The pseudo-code for the BMAP implementation² is as follows:

```

begin
Initialize segmentation with k-means algorithm
Find  $\hat{\alpha}$  and  $\hat{\theta}$  using initial segmentation
Set Flips = LARGE and  $\hat{\beta} = 0$ 
Until (Flips > threshold)
Flips = 0
For all sites  $i \in I$ 
Find  $\hat{x} = \arg \min_{k \in \Lambda} U_i(x_i = k | \mathbf{y}, \mathbf{x})$ 
If ( $x_i$  is not the previous class at  $i$ )
Flips = Flips + 1
Update  $\beta_i$ 
Repeat
Filter the bias field
Compute  $\hat{\theta}$  using current segmentation
Continue
end
    
```

Because the algorithm minimizes the global energy at each decision taken at a voxel site, if the model is valid for the image data, the segmentation always converges to a minimum energy configuration. This may not be the global minimum depending on the initial configuration. The convergence is ideally achieved when the flips of class labels at voxel sites cease. For peeled head scans, this convergence were achieved in about 20 iterations with a threshold of 20 flips. In the case of head scans, the convergence was slow due to noise in the background class. However, in our experiments, we could terminate after about 40 iterations because the flips of class labels were observed only in the background and did not affect the tissue classification thereafter.

Because the prior model parameters of the initial and final segmentations do not differ significantly, we recommend estimation of prior model parameters from the initial

² C++ codes for both AMAP and BMAP algorithms are freely available from the authors.

configuration and keeping them unchanged during iterations. If the initial k -means algorithm does not render a good segmentation of the images, the assignments of equal prior likelihoods for the tissue classes (i.e. α_{0k} s) may evade segmentation leading to an incorrect configuration. Evaluation of prior parameters at every iteration like in the AMAP algorithm may allow pervasion of dominant tissue classes over the others. The algorithm assumes that the number of tissue classes is known, which is mainly determined by the tissue classes of interest. A number of methods to determine the optimal number of intensity classes for a given image have been presented and discussed in Refs [24,26] and this issue is not addressed here.

4. Experiments

4.1. Three-dimensional SPGR head scans

Ten axial head scans (each consists of 124 slices) of healthy subjects whose ages ranged from 8–14 years were obtained on the same GE 1.5 T Signa scanner at the Clinical Center of the National Institutes of Health (NIH), Bethesda, USA, using a three-dimensional SPGR sequence in the steady state. Imaging parameters were TE = 5 ms, TR = 24 ms, flip angle = 45°, acquisition matrix = 192 × 256, number of repetitions = 1 and field of view = 24 cm. Head scans were shelled and CSF was removed using an active brain template (for details, see Ref. [31]). The images were then segmented for two tissue classes corresponding to white and gray matter using the BMAP algorithm. The original slices, segmentation results and recovered bias fields at five different axial levels of a representative head scan are shown in Fig. 1.

Table 1 shows the measurement and prior model parameters with T_{sk} -means initialization and the final segmentation obtained by the BMAP algorithm. For the bias filter, a moving averaging filter of 13 × 13 × 11 size was used, considering the anisotropy of the voxel dimensions. Experiments with different filter sizes indicated that the final segmentations were robust to slight variations of the filter size.

4.2. Three-dimensional CAPRY head scans

Ten coronal MR head scans³ from six males and four females were acquired at the Massachusetts General Hospital's (MGH) Center for Morphometric Analysis using a three-dimensional T_1 -weighted spoiled gradient echo MRI 3D-CAPRY sequence on an 1.5 T General Electric Signa MR system with the following parameters; TR = 50 ms, TE = 9 ms, flip angle = 50°, field of view = 24 cm, slice thickness = contiguous 3.0 mm, matrix =

256 × 256, number of averages = 1 and number of slices = 60. The images were shelled by hand-tracing the outer boundary of the brain parenchyma by experienced raters. The images were segmented to three classes corresponding to white matter, gray matter and CSF using the BMAP algorithm. Five original coronal slices, their segmentations and the recovered bias fields are shown in Fig. 2. The size of the bias filter was 13 × 13 × 9. The model parameters obtained from the initial T_{sk} -means segmentation and the final BMAP segmentation for the scan are shown in Table 2.

4.3. Three-dimensional FLASH head scans

Twenty-three scans were obtained from the Forschungszentrum, Jülich, Germany on a Siemens 1.5 T machine with a three-dimensional FLASH sequence with the following parameters; TE = 5.0 ms, TR = 40.0 ms, field of view = 24 cm, number of slices = 128, and interslice distance = 1.4 mm. The original sagittal scans were interpolated to an isotropic resolution of 1.0 × 1.0 × 1.0 mm. The images of 256 × 256 × 192 size were segmented with the BMAP algorithm for four intensity classes representing background, gray matter, white matter and CSF. Five axial slices from a representative scan are shown together with their segmentations in Fig. 3. An isotropic averaging filter of size 13 × 13 × 13 was used as the bias filter.

4.4. Three-dimensional MDEFT head scans

Twenty scans of healthy adults aged 20–30 were sagittally obtained using a three-dimensional MDEFT sequence with a segmented k -space acquisition (tau = 650 ms, FOV = 250 × 250 × 192 mm, data matrix 256 × 256 × 128, with 90 and 180° pulses at 5 ms half-sech and 10 ms sech pulses, respectively) at the MRI Center of the Max-Planck-Institute of Cognitive Neuroscience, Leipzig, Germany. The original images were rescaled to an isotropic resolution and then segmented into four intensity classes; background, gray and white matter and CSF. The segmentations of five axial slices and sagittal cross-sections of a representative head scan are shown in Figs 4 and 5, respectively. With continuous tissue regions and smooth edges in both orientations of segmentations, the Figures demonstrate the three-dimensional nature of the BMAP segmentation scheme.

4.5. Comparison of AMAP and BMAP results with manual segmentations

Eleven slices at 10 axial slices apart were selected from a representative peeled head scan from the three-dimensional MDEFT images used in the previous subsection. These slices were hand-segmented for three classes white matter, gray matter and CSF, by a neuroanatomist. The particular image was segmented using the T_{sk} -means, AMAP and

³ These images are freely available from the website of the Center of Morphometric Analysis at Massachusetts General Hospital, <http://neuro-www.mgh.harvard.edu/cma/ibsr>

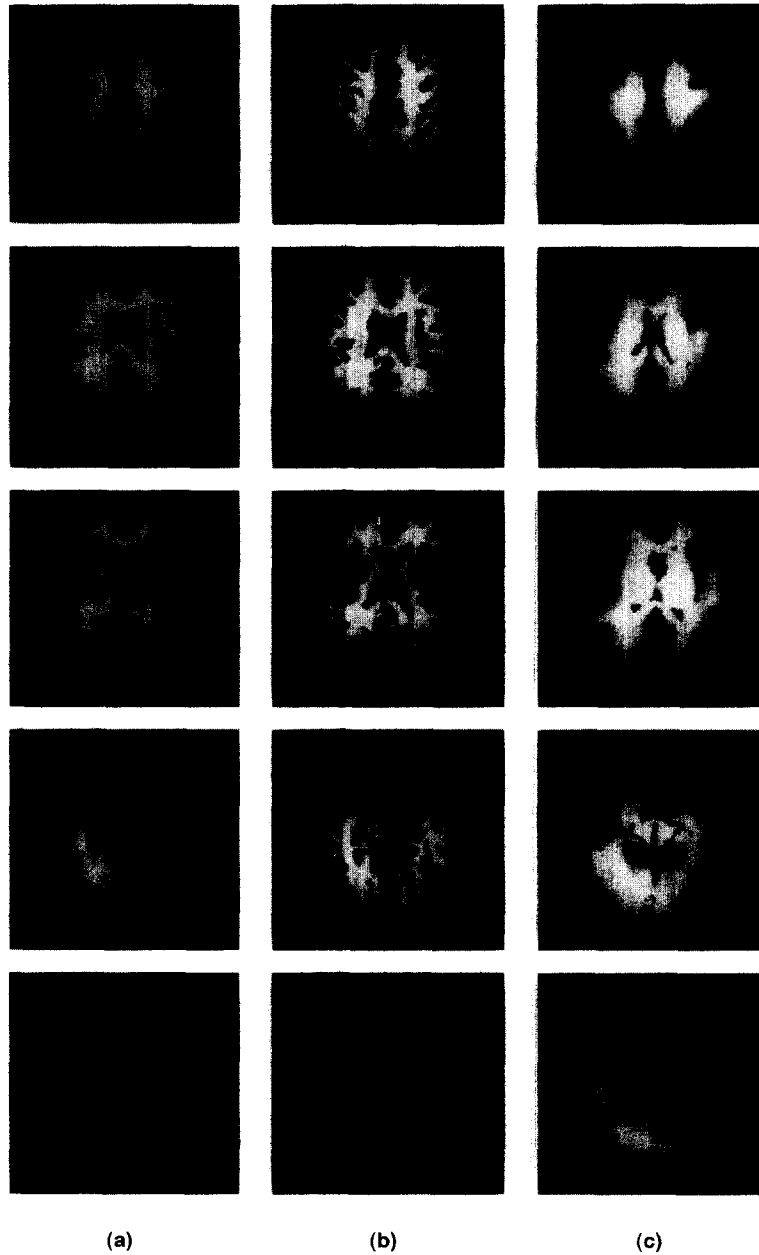


Fig. 1. Illustration of the segmentation of shelled three-dimensional SPGR cerebral MR images into two classes representing white matter and gray matter using the BMAP algorithm: (a) original image slices; (b) segmented slices; and (c) the recovered bias fields at five different axial levels of the brain.

Table 1

The image model parameters obtained for a two-class {Gray matter, White matter} segmentation of a shelled representative three-dimensional SPGR head scans with a T_{sk} -means initialization and the final BMAP segmentation

Model Parameters	Initial (T_{sk} -means)	Final (BMAP)
$(\mu_{\text{Gray}}, \sigma_{\text{Gray}})$	(63.34, 6.16)	(61.23, 13.40)
$(\mu_{\text{White}}, \sigma_{\text{White}})$	(84.0, 6.0)	(96.00, 7.16)
$(\alpha_{0\text{Gray}}, \alpha_{0\text{White}})$	(0.599, 0.401)	(0.522, 0.355)
(α_1, α_2)	(0.706, -0.022)	(0.713, -0.002)
$(\beta_{\text{max}}, \beta_{\text{min}})$	-	(-0.256, 0.188)

BMAP algorithms in three-dimensions. The corresponding 11 slices were extracted and compared with the hand-segmentations. Six slices of hand-segmentations are shown with the corresponding computer segmentations in Fig. 6.

The hand-segmentation was repeated on the same slices once more to measure the reliability of the rater. The correlations between the two attempts (Hand-1 and Hand-2) of hand-segmentations were 94%, 93%, and 96% for CSF, gray matter and white matter, respectively. In Table 3, the total classification errors computed against hand-segmentations over all the 11 slices are given as percentages from the total voxel count. It can be seen that the two attempts of

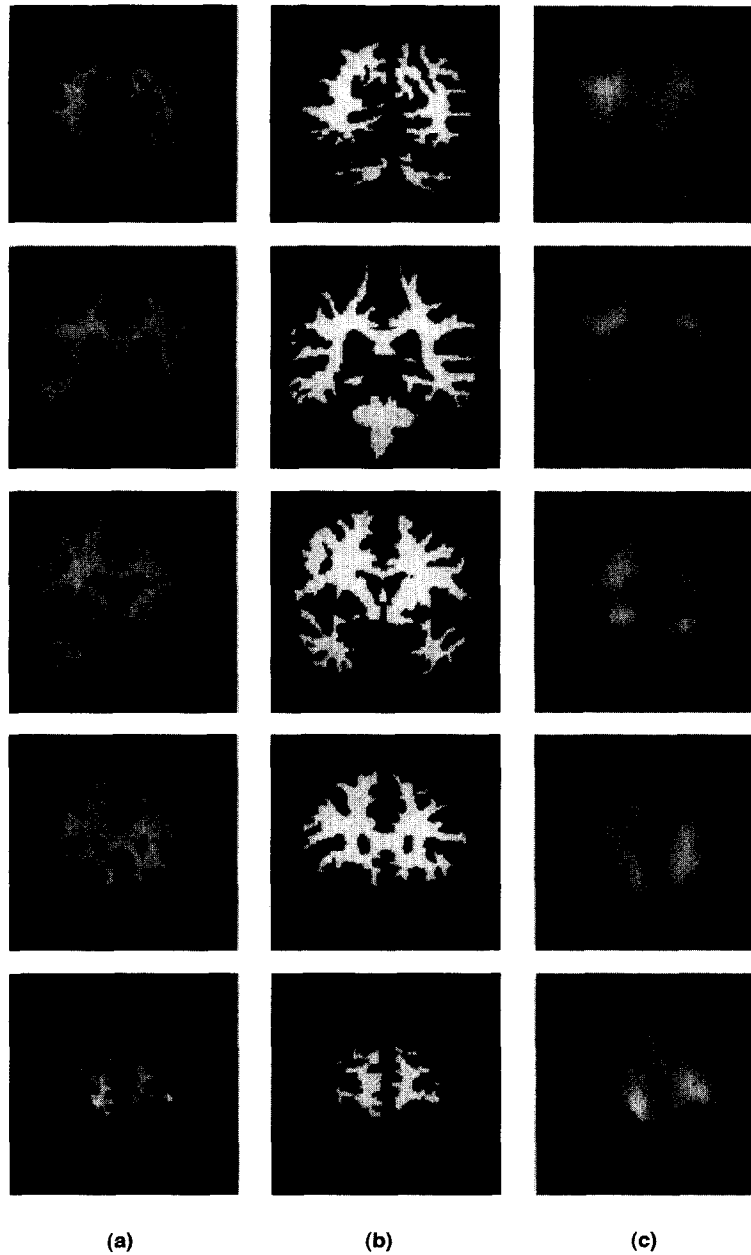


Fig. 2. Illustration of the segmentation of shelled three-dimensional CAPRY cerebral MR images into three classes representing white matter, gray matter and cerebrospinal fluid (CSF) using the BMAP algorithm: (a) original image slices; (b) segmented slices; and (c) the recovered bias fields at five different coronal levels of the brain.

Table 2

The image model parameters obtained for a three-class {CSF, Gray matter, White matter} segmentation of a shelled representative three-dimensional CAPRY head scans with a T_{sk} -means initialization and the final BMAP segmentation

Model Parameters	Initial (T_{sk} -means)	Final (BMAP)
$(\mu_{CSF}, \sigma_{CSF})$	(101.29, 21.74)	(94.05, 19.33)
$(\mu_{Gray}, \sigma_{Gray})$	(148.12, 12.33)	(142.88, 14.38)
$(\mu_{White}, \sigma_{White})$	(191.10, 12.90)	(184.06, 10.92)
$(\alpha_{0CSF}, \alpha_{0Gray}, \alpha_{0White})$	(0.174, 0.453, 0.372)	(0.122, 0.522, 0.355)
(α_1, α_2)	(0.460, -0.020)	(0.569, -0.052)
$(\beta_{max}, \beta_{min})$	-	(-0.268, 0.170)

hand-segmentations differ about 5.8% while the AMAP algorithm shows the best performance with respect to the hand segmentations. An adaptive segmentation scheme recently presented in Ref. [8] was similarly compared with the hand-segmentations by several raters and their error percentages were in the range of (19.45, 23.02). These values are commensurate with the performance of the BMAP algorithm presented here. Superior performance of the AMAP algorithm over the BMAP algorithm, with its brute-force local computations, indicates the limitation of multiplicative assumption to represent the effects of inhomogeneities.

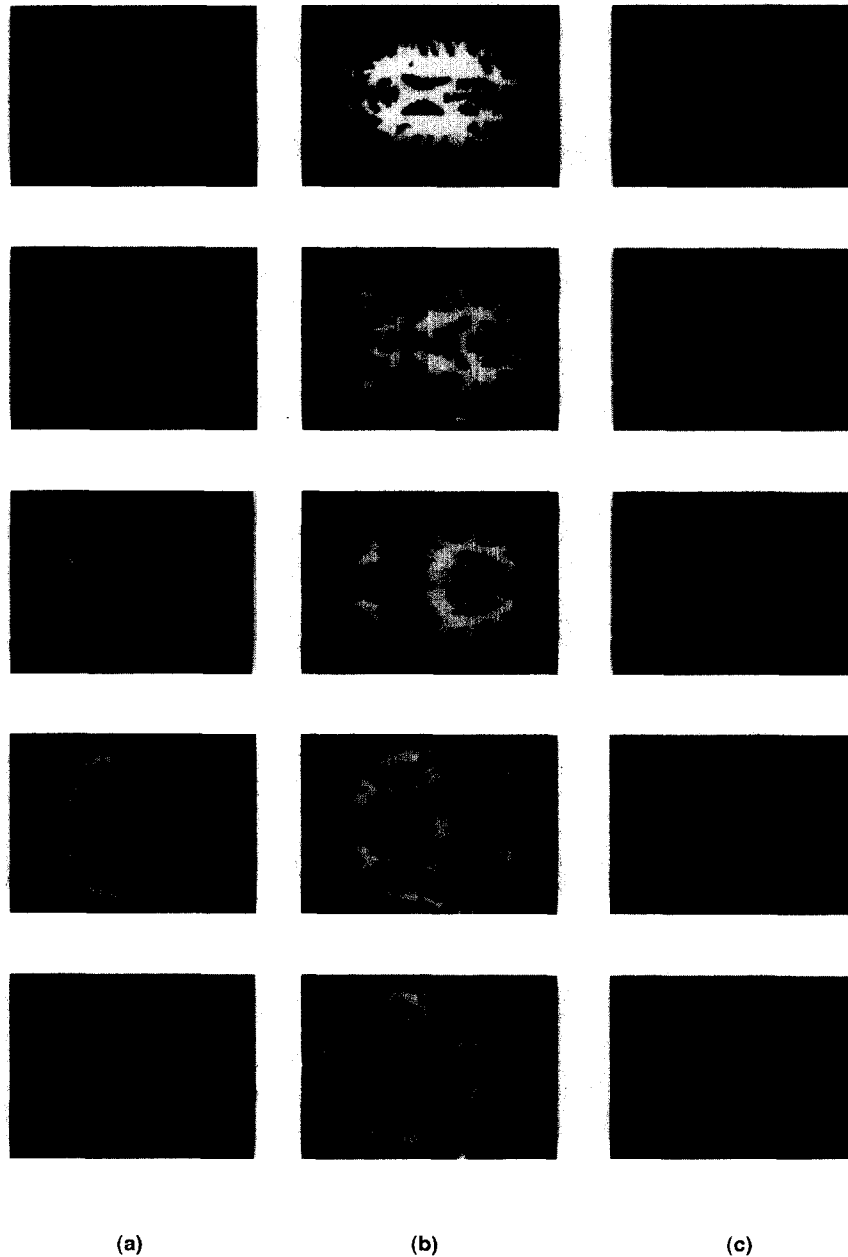


Fig. 3. Illustration of the segmentation of three-dimensional FLASH MR head scans into four classes representing white matter, gray matter, cerebrospinal fluid (CSF) and background using the BMAP algorithm: (a) original image slices; (b) segmented slices; and (c) recovered bias fields at five different axial levels of the brain.

Careful comparisons between computer and hand segmentations reveal that the rater's knowledge of brain anatomy have played a role in the manual segmentation. However, small CSF regions were preserved in automated segmentations, which have not been possible to separate manually. This has contributed to the differences seen in gray matter and CSF volumes. In addition, automated segmentation was performed in three dimensions while the hand-segmentation was performed in two dimensions. It should be noted here that the cortical boundaries given by the BMAP algorithm were very close to those given by the hand traces, but for nuclei such as basal ganglia.

The confusion matrices [32] of the AMAP and BMAP segmentations are shown below, where the rows correspond to the hand-segmented (Hand-1 and Hand-2, respectively) tissue classes with respect to which the hits of the classes in columns of the computer segmentation are counted.

For Hand-1:

	CSF	AMAP Gray	White
CSF	0.838	0.153	0.853
Gray	0.158	0.736	0.106
White	0.004	0.143	0.853

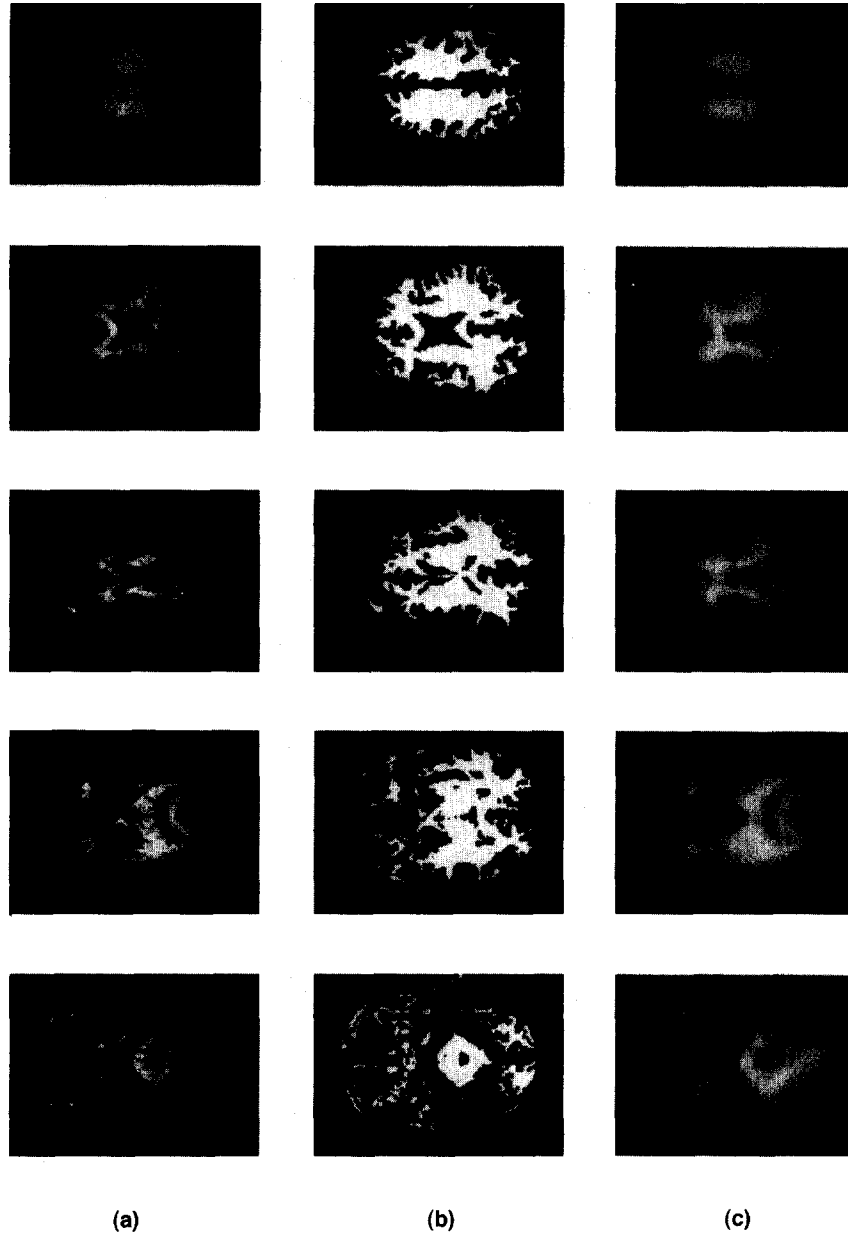


Fig. 4. Illustration of the segmentation of three-dimensional MDEFT MR head scans into four classes representing white matter, gray matter, cerebrospinal fluid (CSF) and background using the BMAP algorithm: (a) the original image slices; (b) the segmented slices; and (c) the bias fields obtained at five different axial levels of the brain.

For Hand-2:

	CSF	BMAP Gray	White
CSF	0.788	0.203	0.009
Gray	0.125	0.844	0.030
White	0.001	0.293	0.706

4.6. Synthetic images

An inhomogeneity profile was simulated using a

two-dimensional rational Gaussian (RAG) function [33]. Given a set of amplitudes $\{V_i; i \in I'\}$, an RAG is defined as:

$$r(u) = \sum_{i \in I'} V_i g_i(u) \quad u \in [0, 1], \tag{26}$$

where $g_i(u)$, the i th basis function of the RAG, is given by $g_i(u) = (G_i(u)) / (\sum_{j \in I'} G_j(u))$ with $G_i(u) = \exp\{- (u - u_i)^2 / (2\sigma_i^2)\}$. V_i , u_i and σ_i represent the maximum value, spatial coordinates of the location of the control points and scale of the i th basis function, respectively. To generate an inhomogeneity field, we selected some control points, generated amplitudes of the control points V_i with a

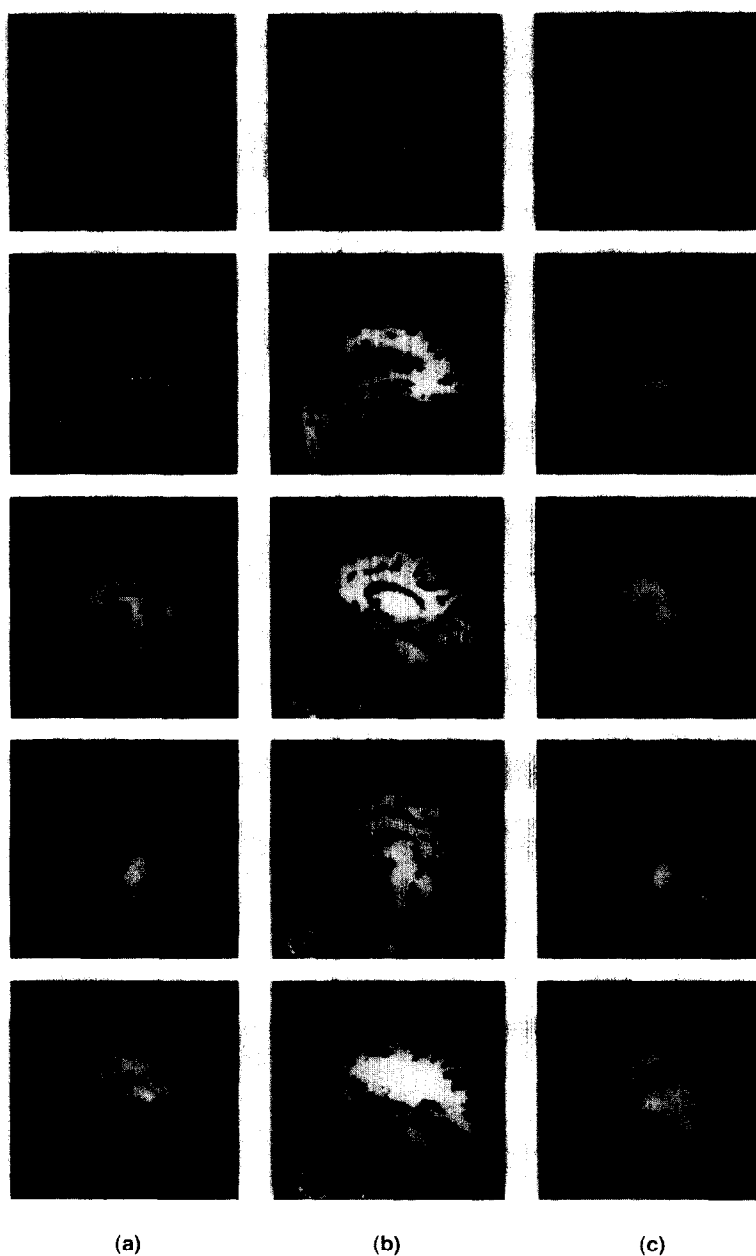


Fig. 5. Illustration of the three-dimensional nature of the BMAP algorithm with sagittal cross-sections of the segmented image in Fig. 4: (a) the original slices; (b) BMAP segmented slices; and (c) the recovered bias fields over five different sagittal sections.

random number generator and calculated the field $r(u)$ over the image domain using Eq. (26).

An axial two-dimensional slice hand-segmented for three tissue classes of a cerebral MR image was obtained to emulate complex shapes of the brain tissue regions. The classes CSF and gray and white matter were given intensity values 1.0, 2.0 and 3.0, respectively. A synthetic MR image was realized by adding the simulated inhomogeneity profile and Gaussian noise to the hand-segmented cerebral image slice. The spacing, between adjacent control points and the scale σ_i in the RAG were selected equal to 16 pixels and the intensity of inhomogeneities was 70% in the uniformity scale [10]. The Gaussian noise had a standard deviation

equal to 0.23 (i.e. $\text{SNR} = 10.17$). The original hand-segmented slice, the added bias field and the synthetic MR image are shown in Fig. 7.

The synthetic MR image was segmented using the BMAP algorithm and other statistical segmentation schemes, namely, T_{sk} -means, fuzzy-c-means [34], MLC, MAP and AMAP. If the bias field was not considered in our model, our algorithm would match the MAP criterion [20] and if the prior model was also not considered, our algorithm would simply equal the ML classification (MLC) [23]. Fig. 8 shows the segmentations obtained using different segmentation schemes. All the algorithms were initialized using a T_{sk} -means algorithm except for fuzzy-c-means

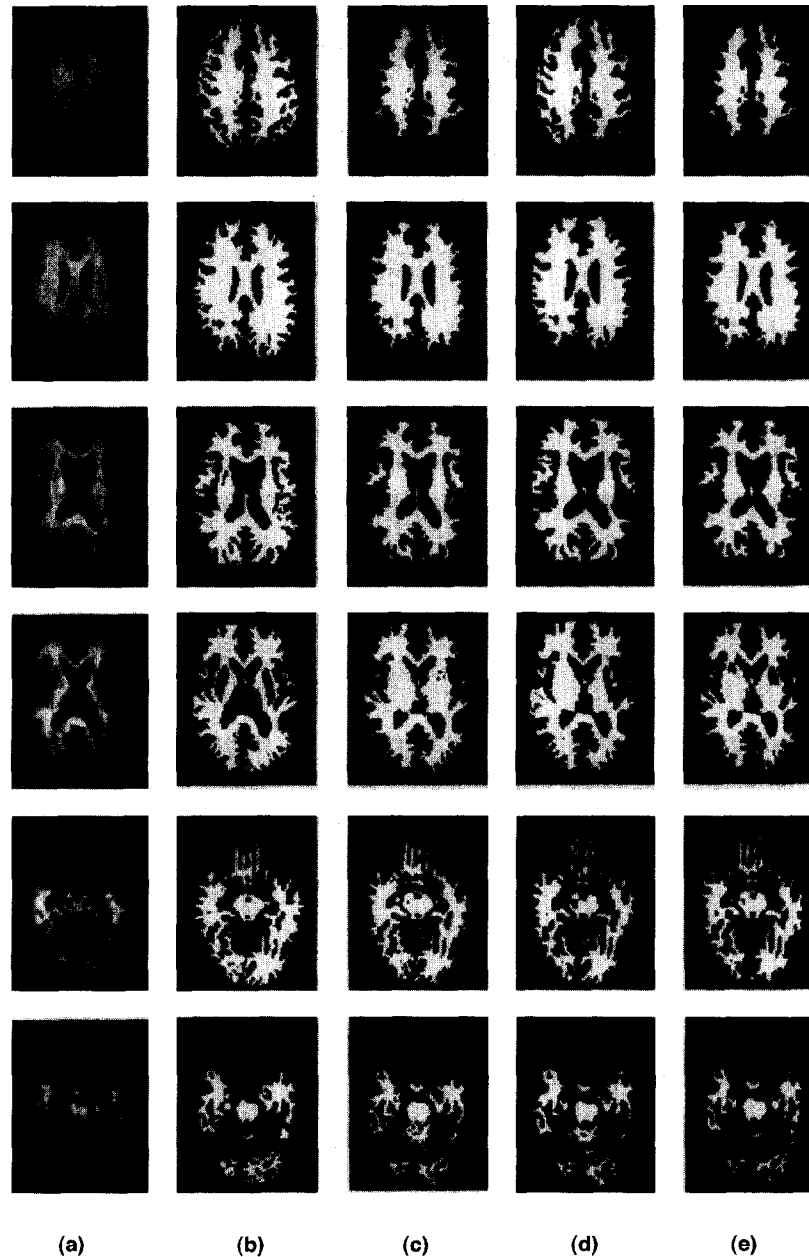


Fig. 6. A comparison of the AMAP and BMAP algorithms with hand-segmented shelled three-dimensional MDEFT head scans: (a) original slices; (b) hand-segmented slices; (c) T_{sk} -means segmentation; (d) AMAP segmentation; and (e) BMAP segmentation.

algorithm and the parameters of the MLC algorithm were obtained using the EM algorithm [19]. The BMAP criteria gave the best segmented image with a two-dimensional averaging filter of size 16×16 . Four nearest neighbors and eight nearest neighbors were considered as the first- and

second-order neighborhoods in the two-dimensional prior model, respectively. The recovered inhomogeneity field by the BMAP algorithm was close to the original and noise showed its random behavior independent of bias field.

To further illustrate the performance of the BMAP algorithm, synthetic MR images were constructed at various levels of inhomogeneities. The segmentation results (number of misclassifications) at various inhomogeneity levels using different schemes are shown in Table 4. At all inhomogeneity levels, the BMAP criteria demonstrated superior performance over all statistical segmentation schemes considered. It was capable of overcoming inhomogeneities up to 70% of signal uniformity which is below the

Table 3
The percentage of the total errors of automated segmentation schemes against the two hand-segmentation attempts (Hand-1 and Hand-2)

Technique	Hand-1	Hand-2	T_{sk} -means	AMAP	BMAP
Hand-1	0.0	5.8	24.0	18.9	21.3
Hand-2	5.8	0.0	24.4	19.1	21.3

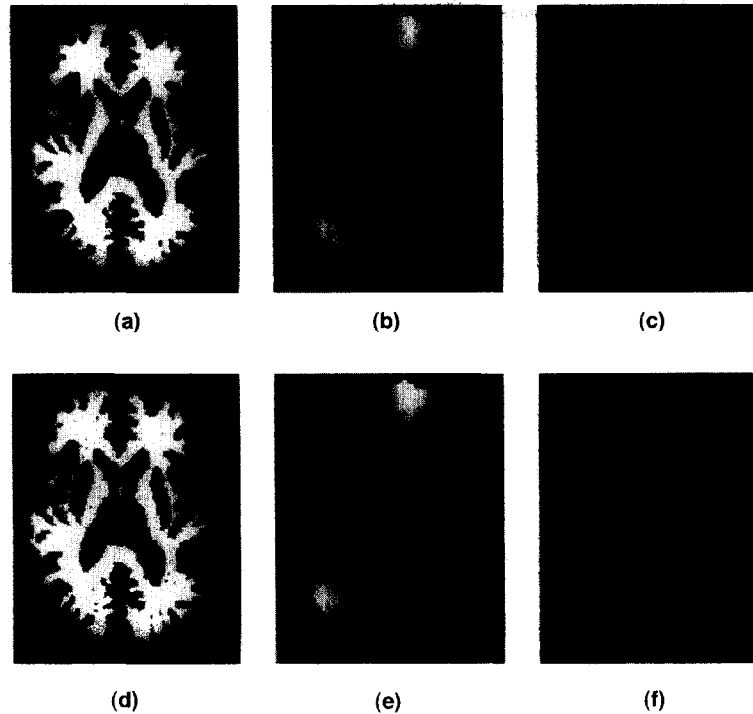


Fig. 7. A synthetic MR image obtained from a hand-segmented axial two-dimensional MR slice to represent gray matter, white matter and CSF: (a) the original hand segmented slice with intensities 1.0, 2.0 and 3.0 given to the three-classes CSF, gray matter and white matter, respectively; (b) a simulated inhomogeneity profile (uniformity = 70%) obtained with a rational Gaussian (RAG) function – the control points were 16 pixels apart in two-dimensions and the scales of the basis functions equal to 16 at all control points; (c) the synthetic MR image obtained by adding the simulated inhomogeneity profile and Gaussian noise equal to 0.23 standard deviation (SNR = 10.17) to the hand segmentation and the (d) segmentation; (e) recovered bias field; and (f) noise profile obtained by the BMAP algorithm.

acceptable limit for clinical scanners. As seen in the table, the BMAP performs better than all other schemes as the intensity inhomogeneities increase. Experiments with different sizes of averaging filter exhibited optimum performance when the filter size was equal to the scale of the inhomogeneities.

5. Discussion

An image model and an algorithm to segment MR images in the presence of noise and inhomogeneities were presented. The proposed model relates the image data to segmentation and inhomogeneities and BMAP algorithm estimates the model parameters from the image data and

utilizes them iteratively to find an optimal segmentation. The proposed scheme is designed to segment MR head scans corrupted by intensity nonuniformities as often encountered in clinical scanners. The intensity inhomogeneities were explicitly represented as a separate bias parameter in the measurement model for each site. The accuracy of the segmentation, of course, depends on the validity of the model for the given image. Because there is no means of measuring the amount of inhomogeneities and gold-standard for the segmentation, it is not possible to assure the accuracy of the segmentation of clinical MR images other than by visual inspection and by comparison with hand-segmented images. The segmentation of cortical gray matter by the BMAP algorithm was near perfect, though it missed some of the subcortical gray structures.

Table 4
Errors in misclassifications per million pixels in the synthetic MR images with different segmentation schemes at different inhomogeneity levels

Algorithm	Intensity of inhomogeneities (uniformity, %)							
	100.0	95.3	90.6	86.0	81.4	76.8	72.3	67.7
T_k -means	21.5	22.0	24.8	31.0	40.5	53.3	77.3	103.5
Fuzzy-c-means	21.7	21.6	24.2	29.4	40.9	54.8	78.9	102.4
MLC	19.9	19.8	22.0	26.6	33.8	43.2	54.8	73.4
MAP	13.1	12.0	12.8	13.2	15.3	22.7	36.3	50.2
AMAP	12.7	11.3	12.3	12.8	14.2	16.2	20.4	30.3
BMAP	11.5	10.8	10.7	10.8	11.4	11.6	11.7	12.3

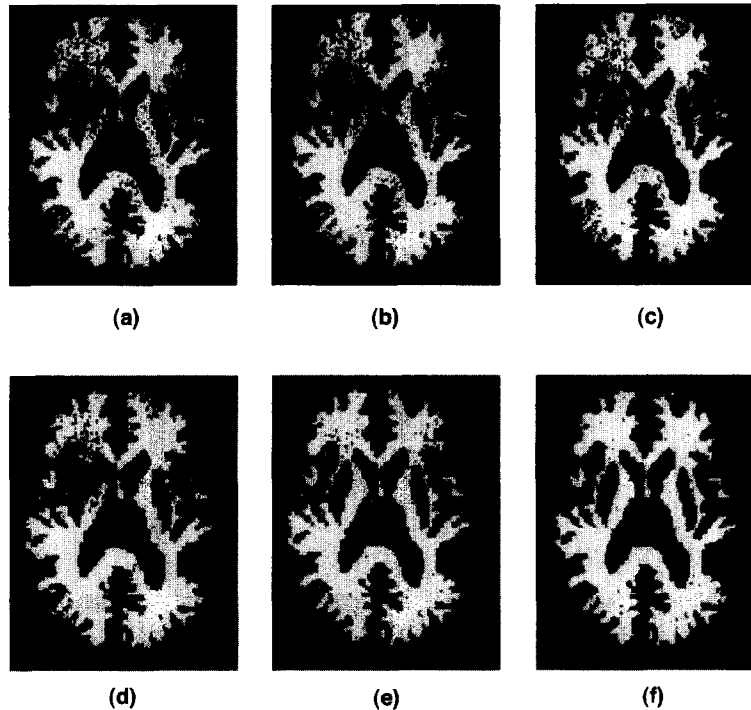


Fig. 8. Segmentation results of the synthetic MR image using: (a) the T_{sk} -means algorithm; (b) the fuzzy-c-means algorithm; (c) the MLC criterion; (d) the MAP criterion; the (e) AMAP algorithm; and (f) BMAP algorithm.

The method was tested over 60 shelled/unshelled MR brain scans obtained from four different clinical scanners. The segmentations were visually and intuitively satisfying for all the scans except for one image with severe inhomogeneities (the particular CAPRY head scan had a rapidly varying inhomogeneity profile due to unknown reasons). The BMAP criterion demonstrated superior performances in the experiments with synthetic images over the T_{sk} -means, fuzzy-c-means, MLC, MAP and AMAP segmentation criteria as the intensity of inhomogeneities increases. The k -means or MLC algorithm is not capable of removing noise and forming connected regions as they do not accommodate for smoothness constraints for segmentation. The classical MAP algorithm does not compensate for the misclassifications introduced by intensity inhomogeneities. The present method accounts for the intensity inhomogeneities as well as smoothness constraints over tissue regions.

In our measurement model, the inhomogeneities were considered to be multiplicative and hence affect the class having the highest intensity, most. Although the multiplicative assumption results in a mathematically sound and tractable model, the reaction between the scanner inhomogeneities and tissue properties may be more complex. Furthermore, the intensity within the same classes may vary depending on the complex properties of tissues. Although a Gaussian random field was used as the prior for the inhomogeneities [8], such a model may not represent the type of inhomogeneities encountered in practical MR scanners. Indeed, a RAG function with basis functions

having random amplitudes generates a realistic inhomogeneity profile similar to those seen in phantom experiments, but the task of finding the parameters of a RAG function given an inhomogeneity profile is difficult. Bias fields obtained from the images in the experiments were close to those recently reported in [9] (unfortunately, the reference provides the bias fields of only simulated images), but different from those seen in phantom experiments. The bias field configurations seem to carry the information of the tissue classes indicating that our definition of the bias field does not solely represent the inhomogeneity profile of the scanner, but as well implicated by the intrinsic properties of the tissues.

The image models of the AMAP and BMAP algorithms differ in the measurement part of the model. The segmentation results of the AMAP algorithms were slightly better than the BMAP algorithm for experiments with hand-segmented peeled images while the BMAP algorithm required less computing resources and times. With K classes, $3K$ parameters (i.e. count, mean and variance) needs to be computed at each site with the AMAP algorithm while only a single parameter (i.e. bias) needs to be computed at each site for the BMAP algorithm irrespective of the number of tissue classes. When three-dimensional head scans are to be segmented for a large number of tissue classes, the AMAP algorithm is not practical and the BMAP algorithm is preferred. Above all, as seen in the experiments with synthetic images, the BMAP exhibited superior performances over the AMAP algorithm in the presence of severe intensity inhomogeneities.

The BMAP segmentation scheme has two drawbacks. Firstly, the segmentation depends on an initial segmentation given by a k -means algorithm. If the initialization is far from the optimal segmentation, the algorithm may end in a local minimum of the energy function. Other optimization criteria such as simulated annealing (SA) [35] may lead to final segmentations independent of the initial segmentation. Given the size of the MR head scans, the SA procedure may not be efficient and practical. The second drawback is the use of the low-pass filter which should ideally give the smoothness constraints of the bias field. A prior model of the inhomogeneities should define this process and an averaging filter delivers only an approximate solution. This approximation is further complicated by the unknown size of the filter which depends on the size of the voxels, the structures aimed at segmentation and the scale of the inhomogeneities. All the parameters of the present model were estimated from the image data using the BMAP algorithm except the size of the bias filter. Because the inhomogeneities in clinical MR images may not have any regularity in both amplitude and scale, an adaptive filter is more appropriate. The time consuming step in the present method is the filtering step which can be easily parallelized on a parallel machine.

Extensions of the present algorithm using rigorous and iterative soft decision schemes such as SA, EM and fuzzy approaches replacing the hard decision schemes like ICM are worth investigating. We have not explicitly taken any precautions to account for the partial volume effects, but with the MRF assumption, the chances of the image elements comprised of white matter and CSF forming thin gray matter edges are rare. Further investigations and improvements of the model are feasible by incorporating interactions among higher-order cliques and neighborhoods and introducing line or surface processes in the MRF model [20].

The present approach attempts to overcome the major stumbling block (i.e. intensity inhomogeneities) for the search of a fully data driven unsupervised method for MR image segmentation. Although only single-channel images were considered, an extension of our approach to multi-channel images [36] is straightforward. Once the decisions about the size of the low-pass filter and the number of classes were made, the BMAP algorithm can be applied to a large database in a robust manner. Our experience states that subtle discrepancies of tissue volumes are possible from MR images of the same subject obtained from different scanners using different MR sequences even with an ideal segmentation scheme. Clinical scanners should appropriately be tuned to accurately depict the tissue characteristics leading to their segmentation and morphometry in a biological sense. Unfortunately, the most of the MR scanning sequences are manufacturer's property and often cannot be replicated on a different scanner barring an unified approach. Nevertheless, the present algorithm, as evidenced by robust and acceptable segmentations of MR images from

four different scanners, is suitable for brain morphometrical studies with clinical MR images disturbed by noise and inhomogeneities of the scanners.

Acknowledgements

The authors wish to thank A.J. Worth of the Center for Morphometric Analysis at Massachusetts General Hospital for providing three-dimensional CAPRY images and the anonymous reviewers whose constructive critics improved the quality of the manuscript.

References

- [1] K. Fitzgerald, Medical electronics, *IEEE Spectrum* 28 (1) (1991) 76–78.
- [2] M.W. Vannier, J.L. Marsh, Three-dimensional imaging, surgical planning and image-guided therapy, *Radiologic Clinics of North America* 34 (3) (1996) 545–563.
- [3] J.C. Rajapakse, J.N. Giedd, J.L. Rapoport, Statistical approach to segmentation of single-channel cerebral MR images, *IEEE Transactions on Medical Imaging* 16 (2) (1997) 176–186.
- [4] K.J. McClain, Y. Zhu, J.D. Hazie, Selection of MR images for automated segmentation, *JMRI* 5 (1995) 485–492.
- [5] B.M. Dawant, A.P. Zijdenbos, R.A. Margolin, Correction of intensity variations in MR images for computer-aided tissue classification, *IEEE Transactions on Medical Imaging* 12 (4) (1993) 770–771.
- [6] C.R. Meyer, P.H. Bland, J. Pipe, Retrospective correction of intensity inhomogeneities in MRI, *IEEE Transactions on Medical Imaging* 14 (1) (1995) 36–41.
- [7] S.K. Lee, M.W. Vannier, Post-acquisition correction of MR inhomogeneities, *Magnetic Resonance in Medicine* 36 (1996) 275–286.
- [8] W.M. Wells III, W.E.L. Grimson, R. Kikinis, F.A. Jolesz, Adaptive segmentation of MRI data, *IEEE Transactions on Medical Imaging* 15 (4) (1996) 429–442.
- [9] R. Guillemaud, M. Brady, Estimating the bias field of MR images, *IEEE Transactions on Medical Imaging* 16 (3) (1997).
- [10] R.R. Price, L. Axel, T. Morgan, R. Newmann, W. Perman, Quality assurance methods and phantoms for magnetic resonance imaging Report of AAPM nuclear magnetic resonance Task Group no. 1, *Medical Physics* 17 (2) (1990) 287–295.
- [11] P.A. Narayana, A. Borthakur, Effects of radio frequency inhomogeneity correction on the reproducibility of intra-cranial volumes using MR image data, *Magnetic Resonance in Medicine* 33 (1995) 396–400.
- [12] J. Haselgrove, M. Prammer, An algorithm for compensation of surface-coil images for sensitivity of the surface coil, *Magnetic Resonance Imaging* 4 (1986) 469–472.
- [13] L. Axel, J. Costantini, J. Listerud, Intensity correction in surface-coil MR imaging, *AJR* 148 (1987) 418–420.
- [14] B.R. Condon, J. Patterson, D. Wyper, A. Jenkins, D.M. Hardley, Image non-uniformity in magnetic resonance imaging – its magnitude and methods for its correction, *The British Journal of Radiology* 60 (1987) 83–87.
- [15] J.C. Bezdek, L.O. Iffall, L.P. Clarke, Review of MR image segmentation techniques using pattern recognition, *Medical Physics* 20 (4) (1993) 1033–1048.
- [16] L.P. Clarke, R.P. Velhuizen, M.A. Camacho, J.J. Heine, M. Vaidyanathan, L.O. Hall, R.W. Thatcher, M.I. Silbiger, MRI segmentation: methods and applications, *Magnetic Resonance Imaging* 13 (3) (1995) 343–368.
- [17] K.O. Lim, A. Pfefferbaum, Segmentation of MR brain images into

- cerebrospinal fluid spaces, white and gray matter, *Journal of Computer Assisted Tomography* 13 (4) (1989) 588–593.
- [18] C. DeCarli, D.G.M. Murphy, D. Teichberg, G. Campbell, G.S. Sobering, Local histogram correction of MRI spatially dependent image pixel intensity nonuniformity, *JMRI* 6 (1996) 519–528.
- [19] A.P. Dempster, L.N. Laird, D.B. Rubin, Maximum likelihood from incomplete data via the EM algorithm, *Journal of the Royal Statistical Society B* 38 (1977) 1–38.
- [20] S. Geman, D. Geman, Stochastic relaxation, Gibbs distribution, and the Bayesian restoration of images, *IEEE Transactions on Pattern Analysis and Machine Intelligence* 6 (1984) 721–741.
- [21] M. Berthod, Z. Kato, S. Yu, J. Zerubia, Bayesian image classification using Markov random fields, *Image and Vision Computing* 14 (1996) 285–295.
- [22] J. Besag, On the statistical analysis of dirty pictures, *Journal of the Royal Statistical Society B* 48 (3) (1986) 259–302.
- [23] R.O. Duda, P.E. Hart, *Pattern Classification and Scene Analysis*, Wiley, New York, 1973.
- [24] J. K Fwu, P.M. Djuric, Unsupervised vector image segmentation by a tree structure–ICM algorithm, *IEEE Transactions on Medical Imaging* 15 (6) (1996) 871–880.
- [25] P. Santago, H.D. Gage, Quantification of MR brain images by mixture density and partial volume modeling, *IEEE Transactions on Medical Imaging* 12 (3) (1993) 566–574.
- [26] Z. Liang, J.R. MacFall, D.P. Harrington, Parameter estimation and tissue segmentation from multispectral MR images, *IEEE Transactions on Medical Imaging* 13 (3) (1994) 339–348.
- [27] A. Lundervold, G. Stovik, Segmentation of brain parenchyma and cerebrospinal fluid in multispectral magnetic resonance images, *IEEE Transactions on Medical Imaging* 14 (2) (1995) 339–348.
- [28] J. Besag, Spatial interaction and the statistical analysis of lattice systems, *Journal of the Royal Statistical Society B* 36 (2) (1974) 192–225.
- [29] S. Lakshmanan, H. Derin, Simultaneous parameter estimation and segmentation of Gibbs random fields using simulated annealing, *IEEE Transactions on Pattern Analysis and Machine Intelligence* 11 (8) (1989) 799–813.
- [30] J. Zhang, J.W. Modestino, D.A. Langan, Maximum-likelihood parameter estimation for unsupervised stochastic model-based image segmentation, *IEEE Transactions on Image Processing* 3 (4) (1994) 404–420.
- [31] J.C. Rajapakse, J.N. Giedd, C. DeCarli, J.W. Snell, A. McLaughlin, Y.C. Vauss, A.L. Krain, S.D. Hamburger, J.L. Rapoport, A technique for single-channel MR brain tissue segmentation: application to a pediatric study, *Magnetic Resonance Imaging* 18 (4) (1996) 1053–1065.
- [32] K. Fukunaga, *Introduction to Statistical Pattern Recognition*, 2nd ed, Academic Press, San Diego, 1990.
- [33] A.E. Goshtasby, Design and recovery of 2-D and 3-D shapes using rational Gaussian curves and surfaces, *International Journal of Computer Vision* 10 (3) (1993) 233–256.
- [34] L.O. Hall, A.M. Bensaid, L.P. Clarke, R.P. Velthuizen, M.S. Silbiger, J.C. Bezdek, A comparison of neural network and fuzzy clustering techniques in segmenting magnetic resonance images of the brain, *IEEE Transactions on Neural Networks* 3 (5) (1992) 672–682.
- [35] S. Kirkpatrick, C.D. Gelatt, M.P. Vecchi, Optimization by simulated annealing, *Science* 220 (4598) (1983) 671–680.
- [36] J.C. Rajapakse, C. DeCarli, A. McLaughlin, J.N. Giedd, A.L. Krain, S.D. Hamburger, J.L. Rapoport, Cerebral magnetic resonance image segmentation using data fusion, *Journal of Computer Assisted Tomography* 20 (2) (1996) 206–218.